Structural and functional correlates of response to deep brain stimulation at ventral capsule/ventral striatum region for treatment-resistant depression

Supplementary Information

Supplementary Methods

Inclusion Criteria: Subjects aged 18-65 years old who were able to provide informed consent were included. Inclusion criteria included psychiatrist-confirmed International Classification of Diseases, 10th revision (ICD-10) diagnostic criteria for major depressive disorder; ≥ 17 on the 17-item Hamilton depression rating scale (HAMD) and medical record documentation that each patient's current major depressive episode persisted for ≥ 2 years or ≥ 4 recurrences with a current episode lasting ≥ 1 year.[1] Treatment resistance was defined as a lack of clinically substantive response to at least 3 or more adequate trials of antidepressant therapy, including 8 or more weeks of 2 or more different classes of antidepressants (eg, selective serotonin reuptake inhibitor, tricyclic antidepressant, tricyclic antidepressant with lithium augmentation, monoamine oxidase inhibitor); at least 1 session of electroconvulsive therapy (ECT), for which the series of ECT was terminated either due to adverse effects or insufficient response (including at least 6 sessions of bilateral ECT), or unable to receive ECT; poor improvement after at least 6 weeks of psychotherapy treatment for the current or a previous depressive episode. Patients who fulfilled the above criteria and remained stable with the current antidepressive regimen for the last month were eligible.

Exclusion criteria were schizophrenia or psychosis unrelated to MDD, severe personality disorder or

neurological disorders (e.g., Parkinson's disease, dementia, epilepsy, tic disorder), organic brain disorders (e.g., tumor, cerebral vascular diseases), history of brain surgery and contraindications for anesthesia or stereotactic surgery. Subjects with contraindications for surgery such as major medical comorbidities or the use of anticlotting medications that could not be discontinued were also excluded.

Post-operative programming: The effectiveness and safety of each electrode contact was assessed by an initial programming session 1 week after the surgery. Trained psychiatrists and neurosurgeons tested each contact individually through careful parameter titration with monopolar stimulation. The amplitude was gradually increased at a 0.5V stepwisely from 2V with fixed frequency (130Hz) and pulse width (90μs). With the stimulator as anode (+), each electrode, beginning with the most distal one, was stimulated as monopolar cathode (−) with an increasing amplitude to a maximum of 6 V for 30-60 s, as long as no acute adverse effects were elicited. If little clinical improvement was achieved following standardized optimization, we tested voltages greater than 6.0 V and adjustments in pulse width and frequency. Induction of beneficial effects or adverse effects were documented. If beneficial effects were noted, the respective electrode was chosen with minimal adverse effect. Chronic stimulation settings were chosen based on the above testing and adjusted every two weeks based on the improvement of depression symptoms.[2]

Image Acquisition: Pre-surgical imaging was performed on a 3T MRI system (Ingenia, Philips Medical Systems, the Netherlands). The MRI protocol consisted of the following sequences: axial three-dimensional T1-weighted Turbo-Field-Echo sequence (TR/TE 6.99/3.42 ms, voxel size 0.75x0.75x1.5mm3, FOV 240x240 mm2), and axial T2-weighted fast spin-echo (T2 TSE; TR/TE 4000/106 ms, voxel size 0.6x0.6x1.5mm3, FOV 240x240 mm2). Postoperative CT scans were also acquired. High-resolution images were acquired on a

LightSpeed16 (GE Medical System, Milwaukee, WI, USA) slice CT with a spatial resolution of 0.49x0.49x0.67mm3. Images were acquired in axial (i.e., sequential/incremental) order at 140 kV and automated mA setting. The noise index was 7.0. A large scan FOV with a 50 cm diameter was used.

DBS Lead Localization: DBS electrodes were localized using Lead-DBS using the PaCER algorithm.[3] In brief, postoperative CT images were first linearly coregistered to preoperative MRI and normalized into ICBM 2009b NLIN asymmetric space using the SyN approach implemented in Advanced Normalization Tools. DBS electrodes were then localized using Lead-DBS and warped into the Montreal Neurological Institute (MNI) space using the PaCER algorithm after visual review and refinement of the coregistrations and normalizations.[4] Anatomical segmentations of local subcortical structures at the DBS site as defined by the CIT-168 atlas.[5]

Electric Fields Estimation: Electric fields (E-fields) were calculated applying a finite element method (FEM)-based model in each patient.[3] Conductivities of 0.33 and 0.14S/m were assigned to gray and white matter, respectively. Based on the volume conductor model, the potential distribution was simulated using the integration of the FieldTrip-SimBio pipeline. The surface of the volume mesh served as the anode. Subsequently, the gradient of the potential distribution was calculated by derivation of the FEM solution.

The anatomical regions defined in AAL-3 used in this study and their abbreviations.

No.	Anatomical description	Abbreviation	No.	Anatomical description	Abbreviation
1	Precentral gyrus	PreCG	30	Fusiform gyrus	FFG
2	Superior frontal gyrus, dorsolateral	SFG	31	Postcentral gyrus	PoCG
3	Middle frontal gyrus	MFG	32	Superior parietal gyrus	SPG

4	Inferior frontal gyrus, opercular part	IFGoperc	33	Inferior parietal gyrus, excluding supramarginal and angular gyri	IPG
5	Inferior frontal gyrus, triangular part	IFGtriang	34	SupraMarginal gyrus	SMG
6	IFG pars orbitalis	IFGorb	35	Angular gyrus	ANG
7	Rolandic operculum	ROL	36	Precuneus	PCUN
8	Supplementary motor area	SMA	37	Paracentral lobule	PCL
9	Olfactory cortex	OLF	38	Caudate nucleus	CAU
10	Superior frontal gyrus, medial	SFGmedial	39	Lenticular nucleus, Putamen	PUT
11	Superior frontal gyrus, medial orbital	PFCventmed	40	Lenticular nucleus, Pallidum	PAL
12	Gyrus rectus	REC	41	Thalamus	THA
13	Medial orbital gyrus	OFCmed	42	Heschl's gyrus	HES
14	Anterior orbital gyrus	OFCant	43	Superior temporal gyrus	STG
15	Posterior orbital gyrus	OFCpost	44	Temporal pole: superior temporal gyrus	TPOsup
16	Lateral orbital gyrus	OFClat	45	Middle temporal gyrus	MTG
17	Insula	INS	46	Temporal pole: middle temporal gyrus	TPOmid
18	Anterior cingulate & paracingulate gyri	ACC	47	Inferior temporal gyrus	ITG
19	Middle cingulate & paracingulate gyri	MCC	48	Anterior cingulate cortex, subgenual	ACCsub
20	Posterior cingulate gyrus	PCC	49	Anterior cingulate cortex, pregenual	ACCpre
21	Hippocampus	HIP	50	Anterior cingulate cortex, supracallosal	ACCsup
22	Parahippocampal gyrus	PHG	51	Nucleus accumbens	Nacc
23	Amygdala	AMYG	52	Ventral tegmental area	VTA
24	Calcarine fissure and surrounding cortex	CAL	53	Substantia nigra, pars compacta	SNpc

25	Cuneus	CUN	54	Substantia nigra, pars reticulata	SNpr
26	Lingual gyrus	LING	55	Locus coeruleus	Red nucleus
27	Superior occipital gyrus	SOG	56	Red nucleus	Locus coeruleus
28	Middle occipital gyrus	MOG	57	Raphe nucleus, dorsal	RapheD
29	Inferior occipital gyrus	IOG	58	Raphe nucleus, median	RapheM

Functional Connectivity Estimation: Voxel-wised functional connectivity seeding from bilateral E-fields were estimated using a normative resting state functional connectivity dataset retrieved from the Brain Genomics Superstruct Project (GSP), which included 1570 subjects in total (ages 18-36), and 1000 subjects (1:1 M/F), were chosen and processed using publicly available tools to generate a normative functional connectivity dataset.[6] The original GSP data was acquired on matched Siemens 3T MAGNETOM Tim Trio MRI systems (Erlangen, Germany) using the vendor-supplied 12-channel phased-array head coil. Preprocessing included global signal regression and spatial smoothing at 6mm full width at half maximum as described.[6] Seeding from voxels within the E-field model, a voxel-wised functional connectivity profile was calculated. Values in E-fields served as weights to generate the connectivity profile using the Lead-DBS tool.[3]

Structural Connectivity Estimation and Fiber Tracking: The structural connectivity estimation and fiber tracking were implemented using Lead-DBS.[3] Briefly, voxel-wised structural connectivity profiles seeding from bilateral E-fields were estimated using a normative group connectome computed based on multishell diffusion-weighted imaging data from 32 subjects of the Human Connectome Project at Massachusetts General Hospital.[7] Whole brain tractography fiber sets were calculated using a generalized q-sampling imaging algorithm. In each subject, 200,000 fibers were sampled and then transformed into MNI space.[7] For each patient, fibers passing through a non-zero voxel of the E-field were selected from this normative connectome

and projected onto a voxelized volume in standard space (2mm resolution) while keeping count of the fibers traversing each voxel. Each fiber received the weight of the maximal E-field magnitude of its passage and fiber densities were weighted by these values.

Leave-one-out cross-validation: The value of the above connectivity profiles as well as the identified fibertracts in outcome prediction was tested by employing leave-one-out cross-validation to predict out-of-sample outcome data.[7] Firstly, connectivity data seeding from E-field from the #2-71 settings were used to create the combined optimal map, and this map was used to estimate the outcome in setting #1; then connectivity data from the #1, 3-71 settings were used to estimate the outcome in patient #2, and so on. The spatial correlation between the individual patient map and the optimal map, which was expressed as a Spearman's rank correlation coefficient, describes the similarity between a patient's brain connectivity profile and the optimal connectivity profile.[7]

Creation of agreement mask across functional and structural imaging modalities: The R-maps of the two modalities (functional and structural) were superimposed and masked with functional weighted average map to generate the following agreement masks:

1) 'good correlation': areas that were positive in three maps (weighted average $map_{func}>0 \cap$ R-$map_{func}>0 \cap$ R-$map_{struc}>0$; voxels showed functional correlation with E-field and positively correlated with outcome in both functional and structural connectivity);

2) 'good anti-correlation': areas that were positive in structural R-map, but negative in functional weighted average map and R-map (weighted average $map_{func}<0 \cap$ R-$map_{func}<0 \cap$ R-$map_{struc}>0$; voxels showed

functional anti-correlation with E-field but positively correlated with outcome in structural connectivity and negatively correlated with outcome in functional connectivity);

3) 'bad correlation': areas that were positive in functional weighted average map, but negative in functional and structural R-map (weighted average $map_{func}>0 \cap$ R-$map_{func}<0 \cap$ R-$map_{struc}<0$; voxels showed functional correlation with E-field but negatively correlated with outcome in both structural and functional connectivity);

4) 'bad anti-correlation': areas that were positive in functional R-map, but negative in functional weighted average map and structural R-map (weighted average $map_{func}<0 \cap$ R-$map_{func}>0 \cap$ R-$map_{struc}<0$; voxels showed functional anti-correlation with E-field but positively correlated with outcome in functional connectivity and negatively correlated with outcome in structural connectivity).

Compared with previous agreement map,[8] the above 4 subtypes of agreement mask were constructed without assigning connectivity strength and only informed the area but not connectivity strength, because though the presence of a functional connection may depend on the presence of a direct or indirect structural connection, the strength of a functional connection does not need to be directly related to the strength of those structural connections.[9] The agreement masks were combined to mask the functional or structural R-map for outcome prediction.

Automated anatomical labelling atlas 3 (AAL-3) was used for brain parcellation.[10] In addition, functionally defined orbitofrontal and prefrontal regions implicated in TRD including orbitofrontal cortex (OFC), dorsolateral PFC (dlPFC), ventrolateral PFC (vlPFC), and ventromedial (vmPFC) were manually defined and used in previous publications from our group (supplemental materials in Morris et al on manual definitions).[11] We hypothesized that regions retained in the agreement mask could be more specific for clinical outcomes in both modalities.

Supplementary Results

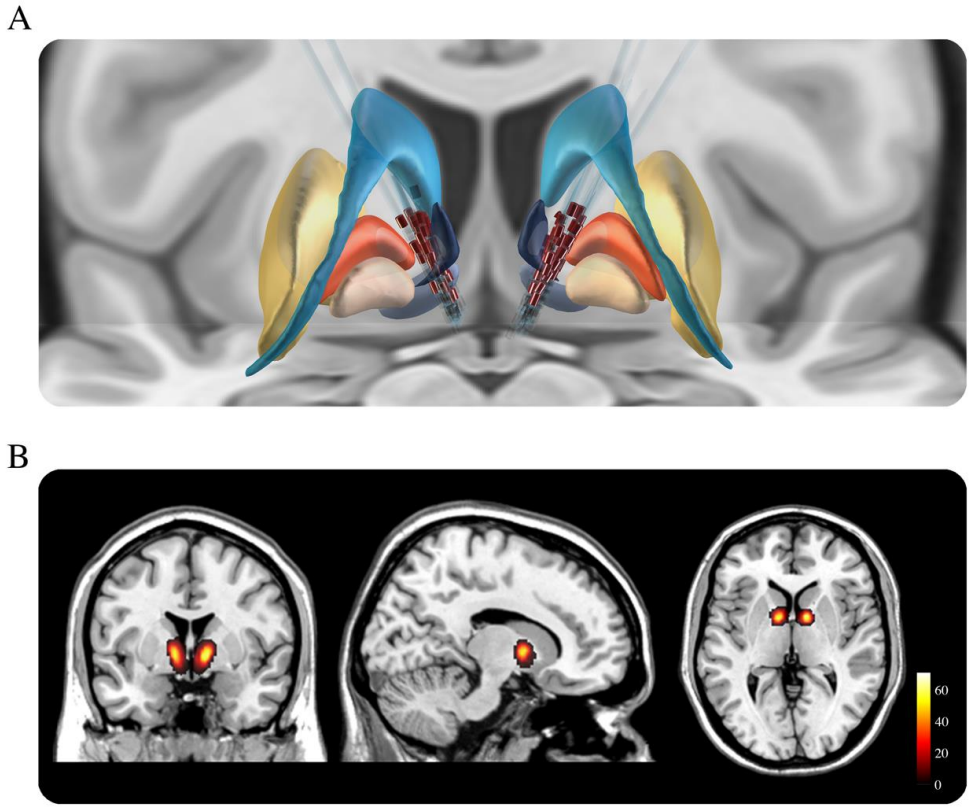

Supplementary figure 1. Location of electrodes the E-fields. A, the current corhort targeting VC/VS, subcortical structures defined by CIT-168 Atlas, with coronal and axial planes of the T1-weighted MNI152 NLIN 2009b template as background. Electrodes were made semi-transparent and active contacts are marked in red, light blue pseudocolor indicates the location of the caudate, yellow for the putamen, orange for the globus pallidus externus, light brown for the globus pallidus internus, dark blue for extensive amygdala, purple for nucleus accumbens. B, location of e-fields in coronal, sagittal and axial T1-weighted MRI (MNI152 NLIN 2009b) slices, the hot map denoted the number of binarized E-fields (thresholded at 0.2V/mm for visualization) overlapped in each voxel.

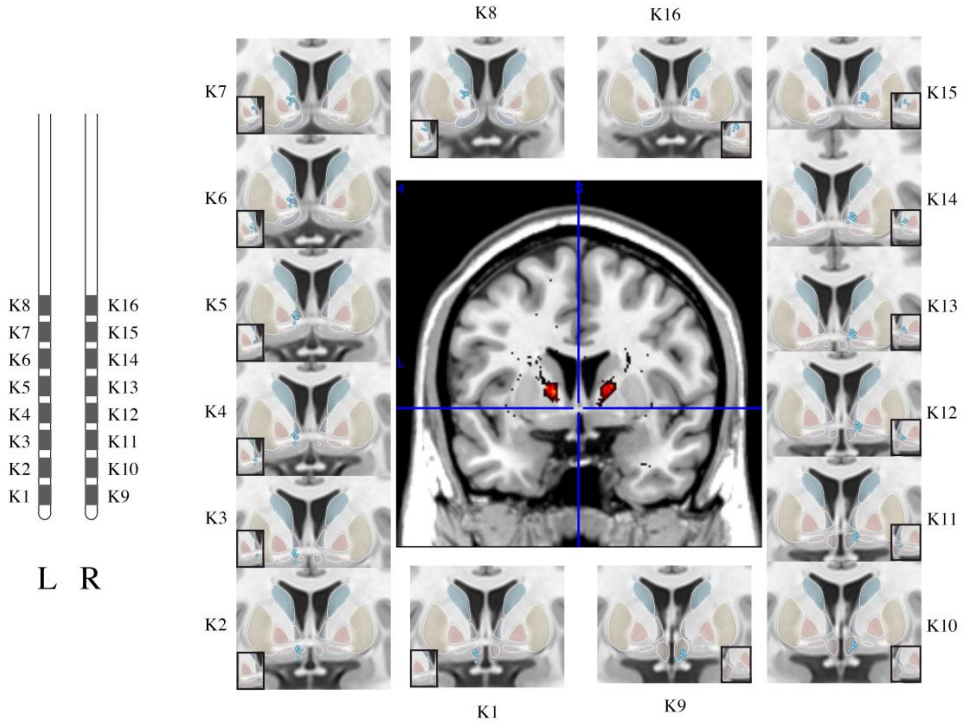

Supplementary figure 2. Contact visualization and fibertracts discriminative of HAMD-17 improvement when modulated. Red tracts in the middle image are positively correlated with clinical improvement. Contacts were shown in blue circles. Active contacts were show in black boxes at the corner of each contact image.

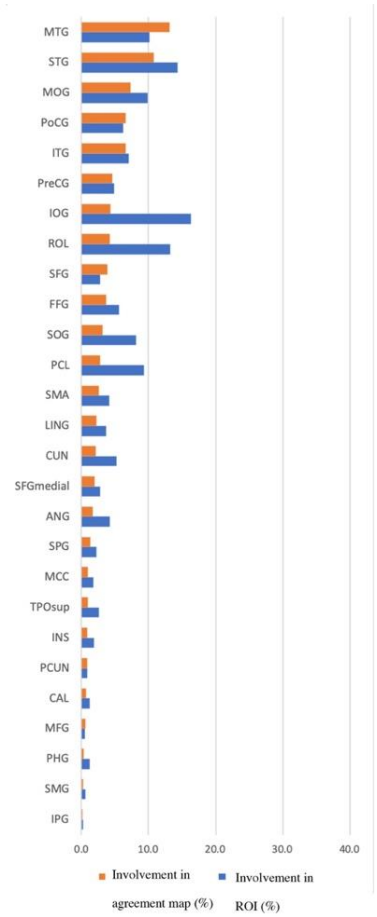

Supplementary figure 3. Percentage involvement in 'good anti-correlation' agreement mask by ROI in AAL-3 brain parcellation. ROIs were analyzed bilaterally.

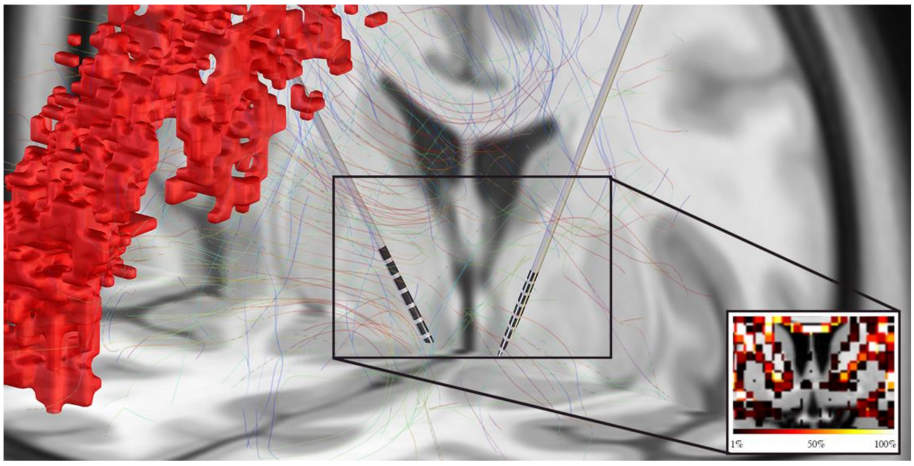

Supplementary figure 4. The whole-brain tractography of the cross-modality map beneficial for outcome in Lead-DBS software. A sample of electrode was displayed. The percent of fibers connected to the voxels relative to the max was denoted by heatmap in the black box.

Reference

1. Hamilton M. A rating scale for depression. *Journal of neurology, neurosurgery, and psychiatry* 1960;23(1):56-62. doi: 10.1136/jnnp.23.1.56.
2. Bergfeld IO, Mantione M, Hoogendoorn ML, et al. Deep Brain Stimulation of the Ventral Anterior Limb of the Internal Capsule for Treatment-Resistant Depression: A Randomized Clinical Trial. *JAMA psychiatry* 2016;73(5):456-64. doi: 10.1001/jamapsychiatry.2016.0152.
3. Horn A, Li N, Dembek TA, et al. Lead-DBS v2: Towards a comprehensive pipeline for deep brain stimulation imaging. *NeuroImage* 2019;184:293-316. doi: 10.1016/j.neuroimage.2018.08.068.
4. Husch A, M VP, Gemmar P, et al. PaCER - A fully automated method for electrode trajectory and contact reconstruction in deep brain stimulation. *NeuroImage Clinical* 2018;17:80-89. doi: 10.1016/j.nicl.2017.10.004.
5. Pauli WM, Nili AN, Tyszka JM. A high-resolution probabilistic in vivo atlas of human subcortical brain nuclei. *Scientific data* 2018;5:180063. doi: 10.1038/sdata.2018.63.
6. Cohen A, Soussand L, McManus P, et al. GSP1000 Preprocessed Connectome. V3 ed: Harvard Dataverse, 2020.
7. Horn A, Reich M, Vorwerk J, et al. Connectivity Predicts deep brain stimulation outcome in Parkinson disease. *Annals of neurology* 2017;82(1):67-78. doi: 10.1002/ana.24974.
8. Sobesky L, Goede L, Odekerken VJJ, et al. Subthalamic and pallidal deep brain stimulation: are we modulating the same network? *Brain : a journal of neurology* 2021 doi: 10.1093/brain/awab258.
9. Straathof M, Sinke MR, Dijkhuizen RM, et al. A systematic review on the quantitative relationship between structural and functional network connectivity strength in mammalian brains. *Journal of Cerebral Blood Flow & Metabolism* 2019;39(2):189-209. doi: 10.1177/0271678x18809547.
10. Rolls ET, Huang CC, Lin CP, et al. Automated anatomical labelling atlas 3. *NeuroImage* 2020;206:116189. doi: 10.1016/j.neuroimage.2019.116189.
11. Morris LS, Kundu P, Dowell N, et al. Fronto-striatal organization: Defining functional and microstructural substrates of behavioural flexibility. *Cortex* 2016;74:118-33. doi: 10.1016/j.cortex.2015.11.004.